

Band tail interface states and quantum capacitance in a monolayer molybdenum disulfide field-effect-transistor

Nan Fang¹ and Kosuke Nagashio^{1,2}

¹Department of Materials Engineering, The University of Tokyo, Tokyo 113-8656, Japan

²PRESTO, Japan Science and Technology Agency (JST), Japan

E-mail: nan@adam.t.u-tokyo.ac.jp, nagashio@material.t.u-tokyo.ac.jp

Abstract. Although MoS₂ field-effect transistors (FETs) with high-*k* dielectrics are promising for electron device applications, the underlying physical origin of interface degradation remains largely unexplored. Here, we present a systematic analysis of the energy distribution of the interface state density (D_{it}) and the quantum capacitance (C_Q) in a dual-gate monolayer exfoliated MoS₂ FET. The C_Q analysis enabled us to construct a D_{it} extraction method as a function of E_F . A band tail distribution of D_{it} with the lowest value of $8 \times 10^{11} \text{ cm}^{-2} \text{ eV}^{-1}$ suggests that D_{it} is not directly related to the sharp peak energy distribution of the S vacancy. Therefore, the Mo-S bond bending related to the strain at the interface or the surface roughness of the SiO₂/Si substrate might be the origin. It is also shown that ultra-thin 2D materials are more sensitive to interface disorder due to the reduced density of states. Since all the constituents for the measured capacitance are well understood, I - V characteristics can be reproduced by utilizing the drift current model. As a result, one of the physical origins of the metal/insulator transition is suggested to be the external outcome of interface traps and quantum capacitance.

KEYWORDS: MoS₂, FET, quantum capacitance, interface states, density of states, MIT

1. Introduction

MoS₂ field-effect transistors (FETs) with high-*k* dielectrics have attracted significant attention in ultimate scaled device research [1-7] because a natural thin body (0.65 nm per layer) is expected to suppress short-channel effects. The electrostatic field-effect control of carriers determines most of the device characteristics and needs to be fully understood before exploring the underlying physics of the electrical transport properties. For example, metal-insulator-transition (MIT) is widely studied in MoS₂ and other two-dimensional (2D) materials [3,8-10]. However, a poor understanding of high-*k*/MoS₂ interface properties might result in an erroneous subsequent physical analysis because the field-effect control by the gate is extrinsically affected by the interface states density (D_{it}), which may arise from the defects in MoS₂ and/or dangling bonds in high-*k* oxides. Specifically, detailed observation via scanning transmission electron microscopy (STEM) and scanning tunneling microscopy (STM) has indicated the existence of sulfur vacancies on the order of $\sim 10^{13} \text{ cm}^{-2}$ in mechanically exfoliated and chemically vapor deposited (CVD) MoS₂, which introduce defect states below the conduction band according to the density functional theory (DFT) calculation [11-13] and severely degrade its electrical properties [14-17]. However, it has not yet been determined whether the electrically activated interface states originate from defect states corresponding to S vacancies because they were evaluated as a function of gate voltage instead of the Fermi energy (E_F).

Moreover, the field-effect control by the gate is reduced intrinsically due to the small density of states (DOS) of thin MoS₂ [18,19]. Extra kinetic energy is required to induce carriers in the MoS₂ channel, which introduces quantum capacitance ($C_Q = e^2 DOS$). The evolution of equivalent circuits from bulk MoS₂ to monolayer MoS₂ is shown in **figure S1**. The capacitance for the multilayer MoS₂ consists of both the depletion capacitance (C_{Dep}) and C_Q in series, whereas C_Q is the only constituent for monolayer MoS₂ because C_{Dep} becomes so large that it can be neglected. Here, capacitance-voltage (C - V) measurement is powerful for directly probing both C_Q and D_{it} , which results in the full understanding of the mechanism of field-effect control [20,21]. Although researchers have attempted to extract D_{it} as a function of E_F for multilayer and monolayer MoS₂ with both the capacitor structure [10,17,22,23] and FET [16,24-26] structure by C - V measurements, the lack of a detailed study on C_Q makes the D_{it} energy distribution questionable. Based on the DOS of 2D materials and the Fermi distribution, C_Q is theoretically formulated for the MoS₂ monolayer [19], but it is neither measured well nor fitted experimentally [24]. One of the main reasons is the lack of consideration of how the interface trap capacitance ($C_{it} = e^2 D_{it}$) affects C_Q extraction. Therefore, to elucidate all the constituents of

the electrostatic field-effect control, focus should be on monolayer MoS₂, which finally results in the understanding of the whole picture of transport properties in the MoS₂ FET.

In this work, the systematic investigation of C - V and current-voltage (I - V) measurements of the same samples is carried out based on relatively high quality monolayer mechanically exfoliated MoS₂ FETs. The interface properties are evaluated as a function of E_F to elucidate the physical origin of interface degradation. A band-tail-shaped D_{it} is observed with the lowest value of $8 \times 10^{11} \text{ cm}^{-2} \text{ eV}^{-1}$ for the monolayer MoS₂. With careful consideration of the effect of interface states, C_Q is clearly extracted experimentally over the temperature range of 75-300 K for the first time. The correlation between top gate bias (V_{TG}) and E_F is obtained via the C_Q analysis. Having evaluated C_{it} and C_Q quantitatively by C - V measurements, I - V characteristics are then well reproduced and understood by utilizing the drift current model. The origin of MIT in monolayer MoS₂ is finally discussed and is suggested to be the external outcome resulting from C_{it} and C_Q .

2. Results and discussion

In this paper, monolayer MoS₂ films were mechanically exfoliated onto the SiO₂ (90 nm)/ n^+ -Si substrate from natural bulk MoS₂ flakes. Raman spectroscopy and atomic force microscopy (AFM) were employed for determining the layer number (Details are shown in **figure S2**). Ni/Au was deposited as source/drain electrodes. Then, Y metal with a thickness of 1 nm was deposited via thermal evaporation of the Y metal from a PBN crucible in an Ar atmosphere with a partial pressure of 10^{-1} Pa, followed by oxidization in the laboratory atmosphere at room temperature to form the buffer layer [27,28]. The Al₂O₃ oxide layer with a thickness of 10 nm was deposited via atomic layer deposition, followed by the Al top-gate electrode formation. I - V and C - V measurements were conducted using Keysight B1500 and 4980A LCR meters, respectively. All electrical measurements were performed in a vacuum prober with a cryogenic system.

2.1. D_{it} extraction from $S.S.$ in I - V

Figure 1 shows a schematic drawing and optical image of the dual-gate monolayer MoS₂ FET. It should be noted that a monolayer MoS₂ with a large area ($>30 \mu\text{m}^2$) was selected for device fabrication and characterization because the measured capacitance should be larger than the stray capacitance (~ 10 fF) of the measurement system. **Figure 2a,b** shows the I_{DS} - V_{TG} characteristic at $V_{DS} = 0.1$ V as a function of V_{TG} for three different MoS₂ FET samples measured at room temperature. The device performance is often scattered from device to device, indicating relatively low reliability of monolayer MoS₂. The top gate oxide capacitance (C_{TG}) can be determined by the relative ratio of capacitive coupling between the top and back gates with a MoS₂ channel (Details are provided in **figure S3** and the extracted physical properties are summarized in **table S1**). According to the C_{TG} value, the two-probe field effect mobilities (μ_{FE}) for samples 1, 2 and 3 are estimated to be 9.5, 6.0 and 2.0 $\text{cm}^2 \text{ V}^{-1} \text{ s}^{-1}$, respectively. Although the mobility is largely underestimated due to the access region, as indicated in **figure 1b**, and the contact resistance, its difference among these three samples still indicates the difference in their interface properties. Indeed, the sample with the highest mobility (sample 1) exhibits the sharpest subthreshold region, in other words, the smallest subthreshold swing ($S.S.$). The $S.S.$ values for the I_{DS} range of $10^{-11} \sim 10^{-10}$ A for samples 1, 2 and 3 are estimated to be 110, 300, 300 mV/dec, respectively. Since $S.S.$ depends on V_{TG} , D_{it} can be precisely extracted as a function of $V_{TG} - V_{TH}$ in the subthreshold region based on $S.S.$, as shown in **figure 4d**, where V_{TH} is the threshold voltage (Details are provided in **note S1**). The sample with the highest mobility has the lowest D_{it} level within the smallest V_{TG} range.

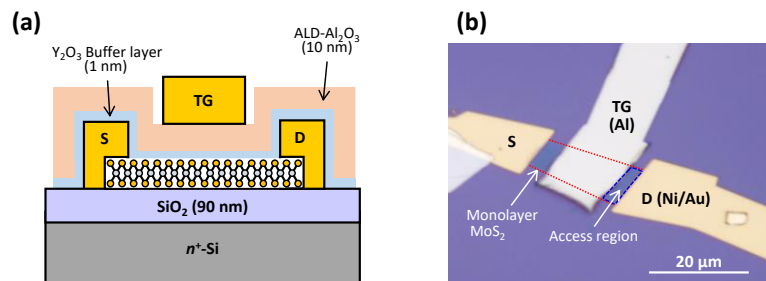


Figure 1. (a) Schematic diagram of the dual-gate monolayer MoS₂ FET. S, D and TG indicate the source, drain and top gate electrodes, respectively. (b) Optical image of the device. The access region refers to the channel region not covered by the top gate electrode.

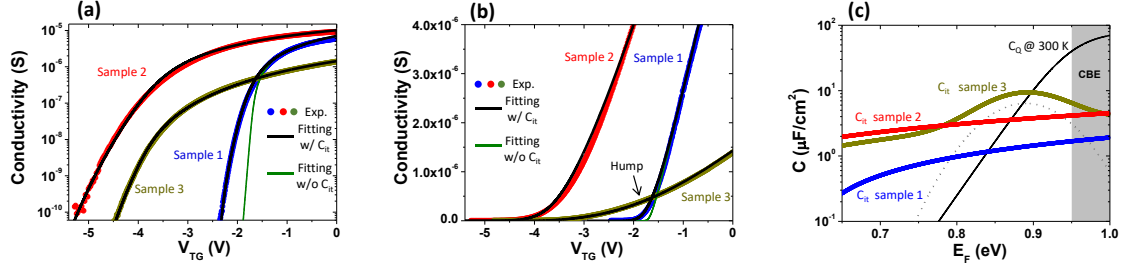


Figure 2. (a) Subthreshold transport characteristics of three different MoS₂ FET samples ($V_{DS} = 0.1$ V). All data are measured at room temperature. No leakage current through the top gate is detected, which is the noise level (\sim pA) for the entire V_{TG} range. (b) Linear scale of (a). (c) Three kinds of C_{it} and C_Q as a function of E_F used for I - V modeling of samples 1-3. Band-tail-shaped C_{it} are assumed for all the samples, which corresponds to the C_{it} level extracted experimentally by the C - V measurement. An additional C_{it} peak with a Gaussian distribution at the peak energy of 0.1 eV below the CBE is introduced for sample 3, which corresponds to the observed hump.

2.2. D_{it} extraction from the equivalent circuit analysis of C - V

The interface properties are studied via capacitance measurement for the same three samples. **Figure 3** shows corrected C_{total} - V_{TG} curves for the frequency range of 1 kHz - 1 MHz. Parasitic capacitance (C_{para}) was carefully considered and removed (details are provided in **figure S4**). Ideally, the measured capacitance (C_{total}) is zero in the deep depletion region, that is, in the off state for the I - V , and saturates asymptotically to C_{TG} in the strong accumulation region because C_Q ($\sim 84 \mu\text{F}/\text{cm}^2$) for monolayer MoS₂ in this region is much larger than C_{TG} . Therefore, all of the C - V curves at different frequencies were shifted to start from zero in the off state. This procedure is reasonable because the C_{TG} obtained in the strong accumulation region after this correction is consistent with the C_{TG} estimated from capacitive coupling between the top gate and back gate in the I - V within a 10% error. Hereafter, C_{total} is defined as the measured capacitance without C_{para} . Frequency dispersion is observed in **figure 3** for all the samples. Observed frequency dispersion clearly indicates the interface quality of measured samples. Specifically, the sample with best interface quality (sample 1) has smallest frequency dispersion. In general, frequency dispersion has two origins. One comes from large C_{it} , which reveals the interface property directly [16]. The other comes from series resistance effect [17], even though the ohmic contacts are realized by the Ni/Au contact (Details are provided in **figure S5**). However, the large C_{para} from SiO₂/ n^+ -Si substrate prevents us from extracting correct conductance signals. The quantitative analyses of series resistance effect is beyond the scope of this paper. The next task is to separately and quantitatively clarify C_{it} and C_Q .

To quantitatively estimate the value of D_{it} via its frequency response, the capacitance is measured as a function of frequency (f). The equivalent circuit is modeled as shown in **figure 4a**. C_{total} can be calculated based on the following equation:

$$\begin{aligned} 1/C_{total} &= 1/C_{TG} + 1/(C_Q + C_{it}) \\ &= 1/C_{TG} + 1/[C_Q + e^2 D_{itA} (2\pi f \tau_{itA})^{-1} \arctan(2\pi f \tau_{itA}) + e^2 D_{itB} (2\pi f \tau_{itB})^{-1} \arctan(2\pi f \tau_{itB})] \end{aligned} \quad (1)$$

where τ_{it} is the time constant for D_{it} , and A and B refer to two types of interface states. This equation is slightly different from that used in a previous paper for a CVD monolayer MoS₂ FET [16] because the multi-level model is more practical than the single-level model [20]. **Figure 4b** shows the C_{total} - f curves at different V_{TG} for sample 1. C_{total} decreases with increasing frequency because C_{it} is unable to completely respond at high frequency. Therefore, $1/C_{total}$ saturates to

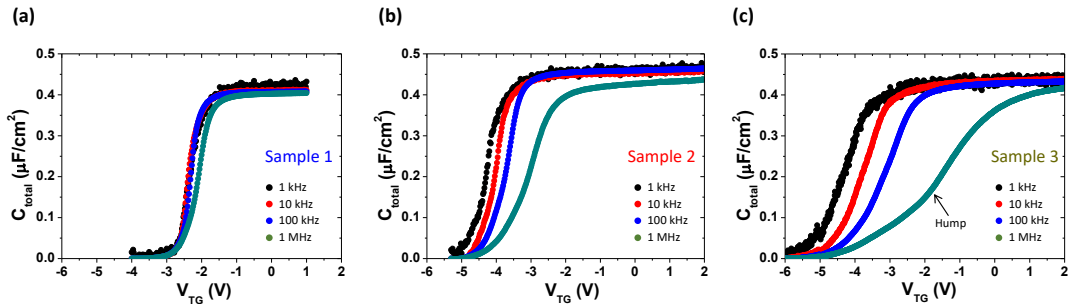


Figure 3. C - V characteristics of (a) sample 1, (b) sample 2, and (c) sample 3 with a frequency ranging from 1 kHz to 1 MHz. There is a clear correlation between the $S.S.$ in the I - V characteristics and the degree of frequency dispersion.

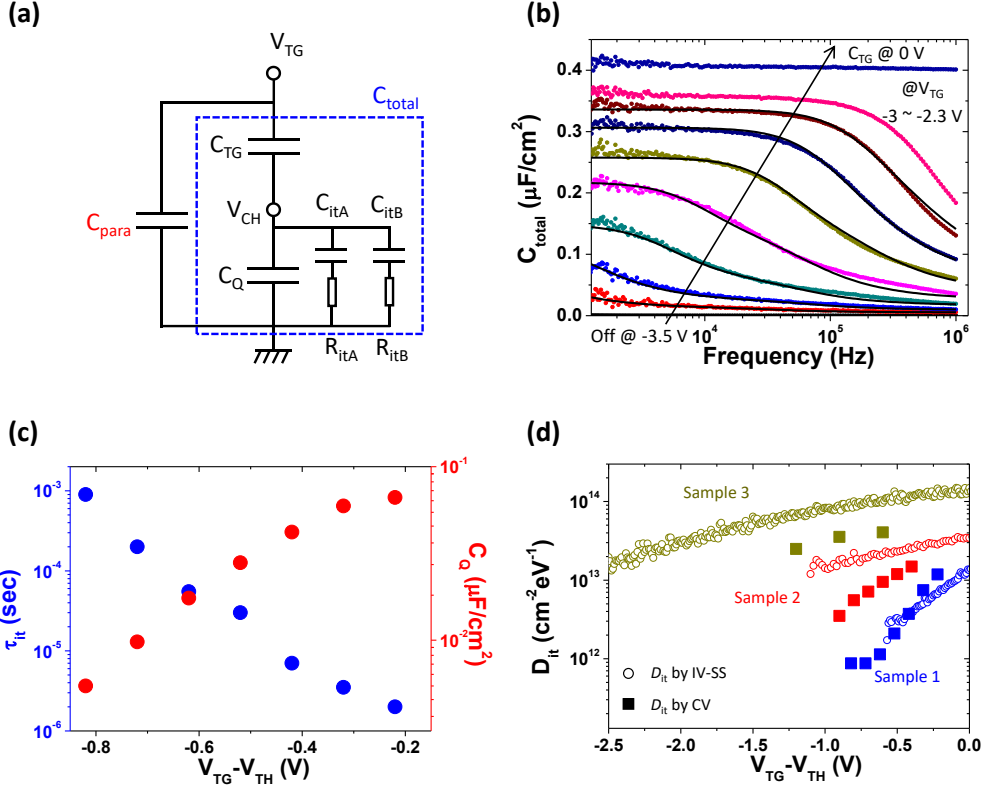


Figure 4. (a) The equivalent circuit model of the device. (b) C_{total} as a function of frequency at different V_{TG} (-3.0~-2.3 V with a step of 0.1 V) for sample 1. Solid circles are the experimental data, and black lines are the fitting curves generated via eq. (1). (c) Extracted τ_{it} and C_{Q} as a function of $V_{\text{TG}}-V_{\text{TH}}$ for sample 1. (d) Extracted D_{it} from both the C - V and I - V as a function of $V_{\text{TG}}-V_{\text{TH}}$ for the three samples.

$1/C_{\text{TG}} + 1/C_{\text{Q}}$ at the high frequency limit according to eq. (1). By using C_{Q} and two types of D_{it} and τ_{it} as fitting parameters, the experimental data are well reproduced, as shown by the solid black lines. Although the number of fitting parameters is large, the accuracy of the estimated D_{it} and τ_{it} is sufficiently high for quantitative analysis because D_{it} and τ_{it} characterize different physical properties. Although two types of interface states are considered, D_{it} mainly originates from the interface states of type A for most of the measured samples ($D_{\text{itA}} > D_{\text{itB}}$, $\tau_{\text{itA}} > \tau_{\text{itB}}$) (Details are provided in **figure S6**). Thus, D_{itA} and τ_{itA} are simply referred to as D_{it} and τ_{it} . C_{Q} , τ_{it} and D_{it} from this fitting are plotted as a function of $V_{\text{TG}} - V_{\text{TH}}$ in **figure 4c,d**. V_{TH} is theoretically defined as V_{TG} at $C_{\text{Q}} = C_{\text{TG}}$ [19], which will be explained later in the C_{Q} analysis. Both C_{Q} and τ_{it} exhibit an approximately linear relation on the logarithmic scale [29,30]. It should be noted that C_{Q} can only be accurately extracted when the saturation tendency of C_{total} in **figure 4b** is clearly observed, which restricts the V_{TG} range for the C_{Q} extraction. Therefore, considering the C_{total} - f curves for samples 2 and 3 shown in **figure S7**, C_{Q} can be extracted from sample 2 but not from sample 3.

Now, let us compare the D_{it} values extracted from the C - V and I - V measurements. As shown in **figure 4d**, the values of D_{it} are comparable. This indicates that the interface properties were successfully evaluated via the electrical measurements. The lowest D_{it} obtained in this study is $\sim 8 \times 10^{11} \text{ cm}^{-2} \text{ eV}^{-1}$, which is one order of magnitude lower than that of a CVD MoS₂ FET [16]. It is expected that these improved interface properties come from a higher quality of the bulk MoS₂ crystals and the Y₂O₃ buffer layer. The D_{it} tail close to the conduction band is still observed for all samples. It should be noted that D_{it} is still presented as a function of $V_{\text{TG}} - V_{\text{TH}}$, but not E_{F} , because the experimental correlation between V_{TG} and the channel potential (V_{CH} , $E_{\text{F}} = eV_{\text{CH}}$) is not clear. In the next section, the effect of C_{it} on C_{Q} is discussed in detail, and as a result, the relation between V_{TG} and V_{CH} is revealed.

2.3. Quantum capacitance analysis

Quantum capacitance was originally derived from the finite DOS of a 2D electron gas [18,31,32]. In addition, it has been successfully extracted in graphene [33,34]. Here, using the same procedure as for graphene, which is different from the C - f analysis in **figure 4b**, C_{Q} is again extracted as a continuous function of C_{TG} . The samples 1 and 2 are used

for this analysis due to their relatively high qualities. First, C_Q is extracted experimentally from the C - V measurements at 1 MHz in **figure 3** to observe the entire picture. At the high frequency limit of 1 MHz, the interface states are assumed to be unable to respond. Therefore, eq. (1) is reduced to $1/C_{\text{total}} = 1/C_{\text{TG}} + 1/C_Q$ by neglecting C_{it} . Since C_{TG} has already been determined in the strong accumulation region, C_Q for samples 1 and 2 is extracted experimentally as a function of V_{TG} in **figure 5a,b**.

Alternatively, C_Q can be calculated theoretically by considering the Fermi distribution and DOS of 2D materials and is expressed as follows [19]:

$$C_Q = e^2 g_{2D} \left[1 + \frac{\exp(E_G / 2k_B T)}{2 \cosh(eV_{\text{CH}} / k_B T)} \right], \quad (2)$$

where $g_{2D} = g_s g_v m^* / 2\pi\hbar^2$ is the band-edge DOS , and E_G is 1.9 eV for monolayer MoS₂. g_s and g_v are the spin and valley degeneracy factors, respectively. m^* is assumed to be $0.6m_0$, where m_0 is the electron mass in vacuum. The mid gap is defined to be $E_F = 0$ eV. Then, the conduction band edge (CBE) is located at 0.95 eV. In eq. (2), C_Q is expressed as a function of V_{CH} , and the correlation between V_{CH} and V_{TG} is required for comparison with the experiment. Based on the ideal equivalent circuit at the high-frequency limit without C_{it} , the theoretical correlation between V_{CH} and V_{TG} is expressed as

$$V_{\text{TG}} = V_{\text{TG, mid-gap}} + \int_0^{V_{\text{CH}}} (C_Q + C_{\text{TG}}) / C_{\text{TG}} dV_{\text{CH}}, \quad (3)$$

where $V_{\text{TG, mid-gap}}$ is the fitting parameter that refers to V_{TG} at $E_F = 0$ eV. This parameter is used to compensate for the intrinsic n -type doping in MoS₂. By combining eqs. (2) and (3), C_Q is calculated as a function of V_{TG} . The experimental and theoretical C_Q - V_{TG} curves are compared in **figure 5a**. The C_Q - V_{TG} curve of sample 1 fits well with the theoretical curve over the wide range of V_{TG} (-1.8 ~ 0.1 V), while it largely deviates from the theoretical curve for sample 2. However, even for sample 1, the deviation of C_Q can be seen on the logarithmic scale, as shown in **figure 5b**.

The deviations of C_Q from the theoretical curve along the transverse and vertical axes have two different origins. One, for the transverse axis, is the “stretch-out” effect [35]. Although the interface traps do not respond to the alternating current (AC) frequency of 1 MHz with the amplitude of 50 mV in the C - V measurement, they respond to the slowly varying direct current (DC) V_{TG} , which causes the C - V curve to stretch out along the transverse V_{TG} axis as the interface trap occupancy changes with V_{TG} . The other origin, which impacts the vertical axis, is that the high-frequency limit of 1 MHz is not always satisfied since τ_{it} is quite short near the CBE, as shown in **figure 4c**. Thus, the extracted C_Q may partially include the contribution of C_{it} in terms of the vertical axis. As a result, the experimental correlation between V_{CH} and V_{TG} by a conventional high frequency method (the so-called Terman method) [20] needs to be reconsidered. For both cases, interface traps cause deviations from the theoretical C_Q curve in the range of $C_Q < C_{\text{it}}$.

As discussed above, the stretch-out effect and the limitation of the measured frequency complicate the correlation between V_{CH} and V_{TG} . Here, we propose a simple method to determine V_{CH} , i.e., find E_F by using the C_Q values obtained from the C - f analysis in **figure 4c** instead of the C_Q values extracted from the C - V measurement at 1 MHz, because they do not include C_{it} . **Figure 5c** shows the theoretical C_Q - E_F curve calculated via eq. (2). Experimental C_Q values extracted from C - f analysis for samples 1 and 2 are then plotted on the theoretical C_Q - E_F line as the blue open circles and red open triangles in **figure 5c**, which compensates the contribution of stretch out along the transverse axis in the C - V curve. Then, the correlated E_F value can be read by following the arrows. We have to emphasize that C_Q obtained

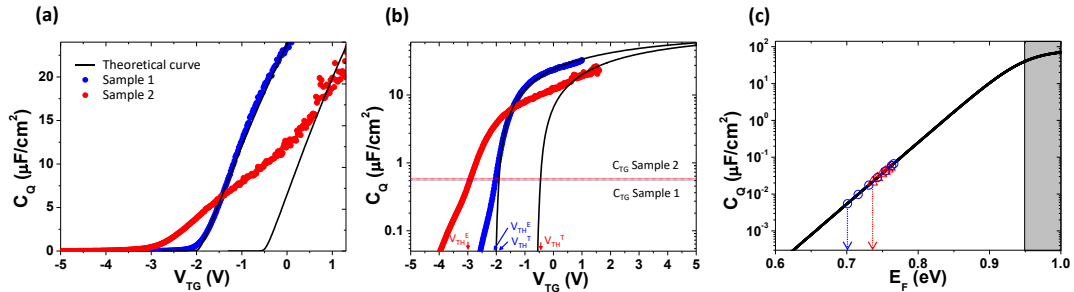


Figure 5. (a) Comparison of experiments and theory for C_Q as a function of V_{TG} for samples 1 and 2. C_Q is experimentally extracted from the C - V curve at 1 MHz. The black line is the theoretical curve calculated based on eqs. (2) and (3). (b) The vertical axis of (a) is converted to the logarithmic scale. V_{TH}^T and V_{TH}^E indicate the theoretical and experimental V_{TH} values, respectively, at $C_Q = C_{\text{TG}}$. (c) Theoretical C_Q - E_F curve used for the correlation between V_{TG} and E_F . Blue open circles and red open triangles indicate experimental C_Q values extracted from the C - f analysis for samples 1 and 2, respectively.

via the C - f analysis is significantly more accurate than that obtained from the C - V curve at 1 MHz because C_{it} can be strictly excluded from C_Q . Sample 2 has a narrower E_F range due to its larger D_{it} . This means that modulation of E_F by V_{TG} is suppressed by a larger D_{it} , which is often referred to as Fermi level pinning at the semiconductor/insulator interface [36,37,38].

The stretch-out effect due to the large D_{it} can be clearly understood by comparing the I_{DS} - V_{TG} curves from figure 2a and the C_Q - V_{TG} curves from figure 5b. Theoretically, V_{TH} is defined by V_{TG} at $C_Q = C_{TG}$ in figure 5b [19]. The V_{TH} determined experimentally for sample 2 is considerably shifted to the negative V_{TG} direction due to stretch out by the large D_{it} . This situation is consistent with the V_{TH} position in the I_{DS} - V_{TG} curve, as shown in figure 2a. It is evident that the apparent V_{TH} position in the I - V is largely affected by the degree of D_{it} .

2.4. Temperature-dependence of C - V & Physical origin for D_{it}

The slope of C_Q becomes sharp at low temperatures due to the intrinsic nature of the Fermi distribution, which provides an alternative means to confirm the validity of C_Q extraction. Based on this idea, both C - V and I - V measurements were performed at 75, 150 and 300 K for an additionally prepared monolayer MoS₂ FET that has a relatively high quality (two-probe mobility ~ 10 cm²V⁻¹s⁻¹, $S.S. = 240$ mV/dec at room temperature).

C_Q is again extracted from the C - V curves at 1 MHz and fitted as a function of V_{TG} at different temperatures, as shown in figure 6a,b. The extracted C_Q - V_{TG} curves are divided into two regions. The first region is the C_Q dominant region, with $C_Q > C_{it}$. In this region, C_Q has a clear temperature dependence and fits well with the theoretical calculation. The other region is the C_{it} dominant region, with $C_Q < C_{it}$. The C_Q - V_{TG} curve deviates from the theoretical curve and shows a gradual change with decreasing temperature. Here, let us consider the V_{TH} shift with decreasing temperature in the C_Q - V_{TG} relation, as shown in figure 6b. It is clear that V_{TH} shifts positively with decreasing temperature due to the temperature dependences of C_Q and D_{it} . This is quite important for studying temperature-dependent transport properties and is discussed later in relation to MIT.

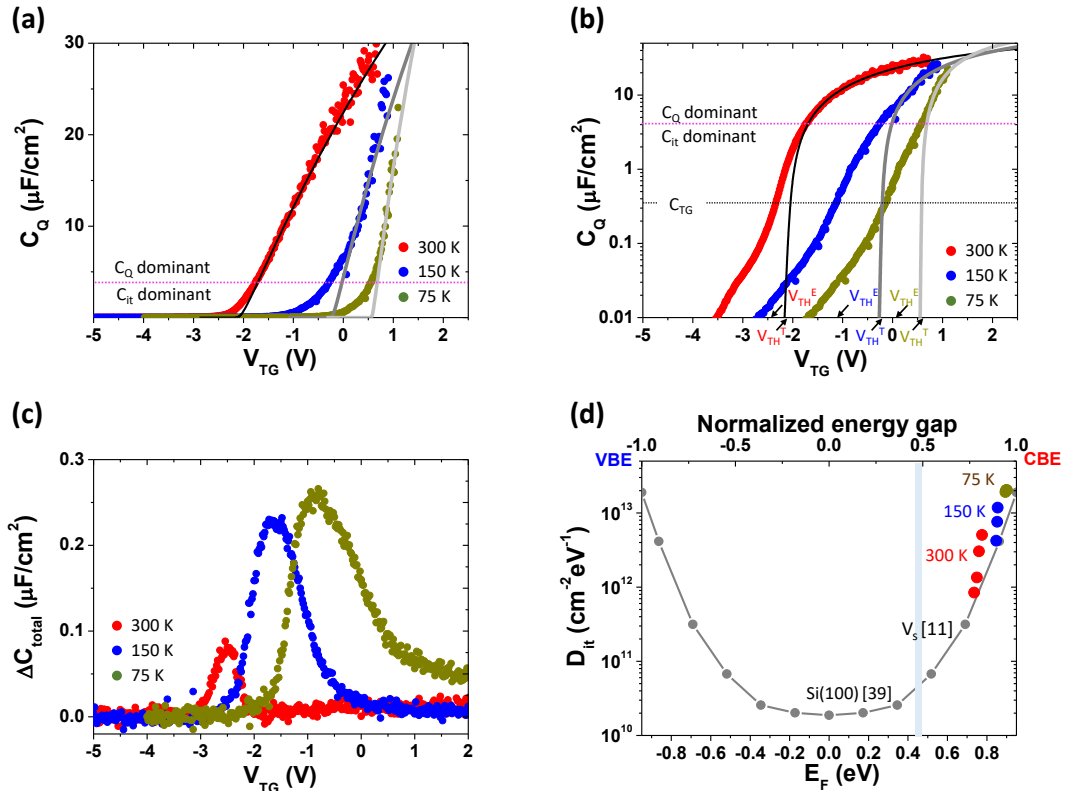


Figure 6. (a) C_Q extracted as a function of V_{TG} at 300 K, 150 K and 75 K for an additionally prepared monolayer MoS₂ FET. Solid lines are the theoretical fitting curves based on eqs. (2) and (3). (b) The same figure as (a) with the logarithmic scale. V_{TH}^T and V_{TH}^E indicate theoretical and experimental V_{TH} values at $C_Q = C_{TG}$, respectively, for different temperatures. (c) ΔC_{total} calculated between 10 kHz and 1 MHz as a function of V_{TG} at different temperatures. (d) D_{it} as a function of E_F . VBE is the valence band edge. For comparison, D_{it} for Si(100) [39] is also included as a function of normalized energy gap (top transverse axis).

To show the frequency dispersion at different temperatures, the capacitance difference (ΔC_{total}) between 10 kHz and 1 MHz as a function of V_{TG} at different temperatures is shown in **figure 6c**. ΔC_{total} gradually increases and broadens with decreasing temperature, which is reasonable for the band tail behavior. The exact D_{it} value is extracted based on eq. (1). Having confirmed the C_{Q} analysis at the measured temperatures, D_{it} is illustrated as a function of E_{F} , as shown in **figure 6d**. In addition, the band tail distribution of D_{it} is successfully confirmed using the temperature-dependent C - V measurements, the results of which are similar to those of the SiO₂/Si case [39].

Let us discuss the physical origin of D_{it} for a monolayer of MoS₂. According to the DFT calculation [11], an S vacancy introduces an isolated D_{it} peak at 0.46 eV below the CBE, which is also indicated in **figure 6d**. It is clear that the present band tail behavior of D_{it} is not directly related to the S vacancy. This band tail distribution of D_{it} , which is also called the U-shaped band edge states, has been widely observed in Si/SiO₂ [39-41], Ge/GeO₂ [42,43] and other conventional oxide semiconductor interfaces [44]. In the case of the Si/SiO₂ interface, many models have been proposed to explain the U-shaped band edge states. For example, the stretched Si-Si bonds at the interface [40] and distortion of the Si-O-Si bond angle [45] are expected to cause trap levels because the conduction band is composed of an anti-bonding state of the sp³ hybrid orbital. The strain is concentrated at the Si/SiO₂ interface due to the density difference. This may cause a deviation of the anti-bonding state energy, resulting in the U-shaped band edge states. Therefore, since the conduction and valence bands of MoS₂ are mainly composed of the energy splitting of the Mo d orbital [11, 46], the Mo-S bond bending due to the strain caused by lattice mismatch at the MoS₂/high- k interface [47,48], the surface roughness of the SiO₂ surface, or bond bending related to the S vacancy might be the origin. However, further study is required to clarify the physical origin of the U-shaped D_{it} in MoS₂.

The interface properties of a bulk MoS₂ capacitor have been measured as an isolated D_{it} peak by using the Terman method [17] and it is suggested that it be ascribed to the S vacancy. Our multilayer MoS₂ FET also shows the hump in C - V curves (data is not shown here). More interestingly, a similar hump is also observed in monolayer MoS₂ with poor interface quality (sample 3), as shown by arrows in the C - V curve of **figure 3c** and the $I_{\text{DS}}-V_{\text{TG}}$ curve of **figure 2b**. Thus, the origin of this hump could be the sulfur vacancy or its derivative (e.g., disulfur vacancy). However, for samples 1 and 2 with relatively high quality interfaces, the hump is not obvious. Since the D_{it} level of the band tail of a monolayer is much higher than that of a multilayer, the high D_{it} level of a monolayer may hide the isolated D_{it} peak of the S vacancy. If this is the case, the observation of the hump in sample 3 suggests that the concentration of S vacancies in sample 3 is highest.

Let us discuss the reason why the C - V curves of a monolayer MoS₂ have a significantly larger frequency dispersion than those of Si even though the D_{it} energy distributions are roughly comparable. One reason is that the large band-gap of the monolayer MoS₂ broadens the D_{it} energy distribution. The most important reason is the smaller DOS of the monolayer MoS₂. As we discussed in the previous section, the effect of C_{it} on C_{total} is determined by the relative ratio of $C_{\text{it}}/C_{\text{Q}}$. When C_{Q} is smaller than C_{it} over a certain energy range, C_{it} degrades the C - V curve in terms of the large frequency dispersion, large V_{TH} shift, limited modulation of E_{F} by V_{TG} , and other factors. In the case of the Si FET structure, semiconductor capacitance is composed of inversion layer capacitance (C_{Inv}) instead of C_{Q} , as shown in **figure S1**. The DOS for Si inversion is much larger than that for the monolayer MoS₂, which suppresses the effect of C_{it} on C_{total} . This is supported by the reduced frequency dispersion in the C - V curve for the multilayer MoS₂ due to the larger C_{Q} . As a result, ultra-thin 2D materials are more sensitive to interface disorder due to reduced DOS .

2.5. C_{Q} and C_{it} effect on I - V characteristics

Since all the constituents in C_{total} are well understood, it is now possible to reproduce I - V characteristics by completing two steps: the determination of the carrier density controlled by the electrostatic field-effect of the top gate, and then, the characterization of the electron transport of these carriers in the conduction band. Therefore, carrier density control by V_{TG} is modeled based on the well-understood equivalent circuit. V_{CH} can be correlated to V_{TG} as follows:

$$V_{\text{TG}} = V_{\text{TG},\text{mid-gap}} + \int_0^{V_{\text{CH}}} (C_{\text{Q}} + C_{\text{it}} + C_{\text{TG}}) / C_{\text{TG}} dV_{\text{CH}}. \quad (4)$$

For this equation, C_{it} is added to eq. (3) because C_{it} is able to respond completely in conventional I - V characteristics due to the DC measurement. The channel carrier density (n_{CH}) - V_{CH} relation is calculated using the equation [19]

$$n_{\text{CH}} = g_{2\text{D}} k_{\text{B}} T \ln \left[1 + \exp \left((eV_{\text{CH}} - E_{\text{CBE}}) / k_{\text{B}} T \right) \right]. \quad (5)$$

Then, the fundamental drift current equation $\sigma = en_{\text{CH}}\mu_{\text{D}}$ is applied to simulate the carrier transport process, where σ and μ_{D} refer to conductivity and drift mobility, respectively. Since $C_{\text{Q}}(E_{\text{F}})$ is analytically calculated, $C_{\text{it}}(E_{\text{F}})$, $\mu_{\text{D}}(E_{\text{F}})$ and $V_{\text{TG},\text{mid-gap}}$ are used as fitting parameters. $\mu_{\text{D}}(E_{\text{F}})$ is assumed to be independent of E_{F} with a constant value for simplicity. Then, the drift mobilities for samples 1, 2 and 3 are estimated to be 12.3, 8.2, 2.3 cm² V⁻¹ s⁻¹, respectively.

Drift mobilities are slightly higher than two-probe field-effect mobilities obtained experimentally (**Table S1**) because C_{it} reduces carrier controllability by the gate even in the linear region of $I_{DS}-V_{TG}$ curves. Although this is a rough assumption, it is valid in the linear region of the $I-V$. Whereas in the subthreshold region, the drift mobility might decrease with reduced screening effect, the dominant factor in determining I_{DS} in this region is the carrier density, which is exponentially related to V_{TG} , instead of the drift mobility. Band-tail-shaped C_{it} curves with three different levels are assumed for the samples, as shown in **figure 2c**. For sample 3, an additional C_{it} peak with a Gaussian distribution at the peak energy of 0.1 eV below the CBE is introduced, which is used to reproduce the hump observed in **figure 2b**. Although the peak energy for a single S vacancy is reported to be 0.46 eV below the CBE by DFT calculation [11], the energy level of the present C_{it} peak is quite shallow, suggesting the existence of clustering of S vacancies [49]. Finally, experimental $I_{DS}-V_{TG}$ characteristics of samples 1, 2 and 3 are well fitted based on the above model, as shown by the black solid lines in **figure 2a,b**. Additionally, an ideal $I-V$ curve without C_{it} for sample 1 is exhibited by the green solid line in **figure 2a,b**, where the ideal $S.S.$ of ~ 60 mV/dec as well as the sharp transition from the linear to the subthreshold region are evident. In this case, V_{TH} can be uniquely determined. However, C_{it} does degrade the subthreshold region, i.e., a $S.S.$ of ~ 100 mV/dec for sample 1 and over 300 mV/dec for samples 2 and 3. This degradation introduces the ambiguity in the V_{TH} extraction by experiment, which has been encountered in the $C-V$ analysis as well.

2.6. Interpretation of MIT

In the final section, let us discuss the contribution of C_{it} to MIT. The top gate FET structure in **figure 1b** is unsuitable for studying $I_{DS}-V_G$ in the linear region precisely due to the existence of the access region, which results in the underestimation of the intrinsic drift mobility in the linear region. Thus, a back-gate four-probe FET with monolayer MoS₂ on 90-nm SiO₂/ n^+ -Si substrate is prepared. The experimental $\sigma-V_{BG}$ curves excluding the series resistance are shown in **figure 7a**. Clear MIT behavior is observed for the present device quality. So far, MIT of MoS₂ has been discussed for both $I-V$ [8,9] and $C-V$ [10] with different models. Here, the temperature dependences of $\sigma-V_{BG}$ curves obtained experimentally are again reproduced by the above-mentioned model using the relation $\sigma = en_{CH}\mu_D$. The temperature dependence of C_Q is calculated in **figure S8a**, which results from the natural property of the Fermi distribution. The band tail shape of C_{it} with three different levels, that is, high, low and no C_{it} , is again assumed in **figure S8a**, while C_{BG} is estimated as 0.038 μFcm^{-2} for back gate SiO₂ oxide with a thickness of 90 nm. $V_{BG, \text{mid-gap}}$, instead of $V_{TG, \text{mid-gap}}$, is constant for all temperatures. Then, n_{CH} can be calculated using eqs. (4) and (5). Moreover, the μ_D used for this modeling is the same for all three C_{it} cases and is slightly larger than the experimental μ_{FE} at all temperatures (Details are shown in **figure S8b**). **Figure 7b** shows simulated $\sigma-V_{BG}$ curves with three different C_{it} levels. MIT is well reproduced using the high C_{it} . By decreasing the C_{it} level, the crossover points of the MIT shift to the negative V_{BG} side and finally enter the subthreshold region for the case with no C_{it} , which blinds the MIT. Recently, no MIT has been reported for an h -BN-encapsulated monolayer CVD-MoS₂ FET [50], suggesting a quite low C_{it} due to superior 2D/2D interface properties.

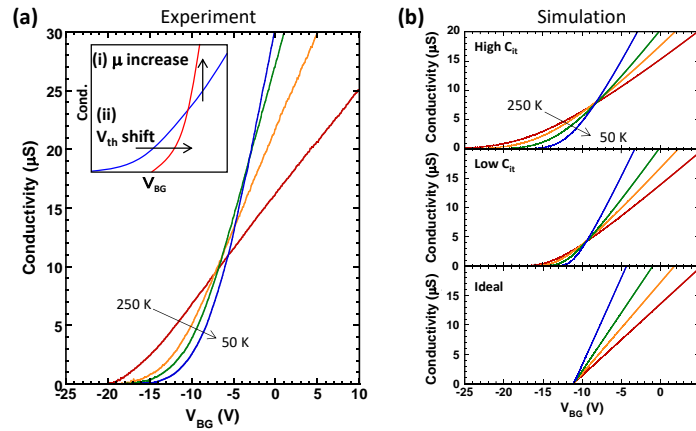


Figure 7. (a) Experimental four-probe conductivity as a function of V_{BG} for a back-gate monolayer MoS₂ FET at 50–250 K, showing the typical MIT behavior. (b) Simulated $\sigma-V_{BG}$ curves with high C_{it} , low C_{it} and no C_{it} (ideal), which are shown in figure S8a. $V_{BG, \text{mid-gap}} = -53$ V, -23 V, and -12 V are assumed for high C_{it} , low C_{it} and no C_{it} , respectively.

Generally, MIT can be observed intuitively by the combination of (i) the increase in the mobility and (ii) positive V_{TH} shift with decreasing the temperature. Within the present model, the mobility is assumed to increase with decreasing temperature due to suppression of phonon scattering, as observed in the experiment. Therefore, the dominant key factor for MIT is a positive V_{TH} shift with decreasing temperature. This occurs because E_F at V_{TH} approaches the CBE at lower temperature. Thus, a larger amount of C_{it} needs to be filled by electrons before reaching V_{TH} at lower temperature. This also explains why V_{TH} shifts more with temperature in the high C_{it} case. So far, many models have been developed for MIT on 2D layered channels. The present model indicates that C_{it} -induced positive V_{TH} shift is one of the main origins for “extrinsic” MIT.

3. Conclusion

The degradation of the electrostatic field-effect control for the monolayer mechanical exfoliated MoS₂ FET is systematically studied using both C - V and I - V characterization in terms of C_Q and C_{it} . C_Q was confirmed over all of the measured temperature ranges (75~300 K). Therefore, D_{it} was evaluated as a function of E_F by the newly constructed C_Q analysis, which can also be applied for other monolayer TMDs. D_{it} was extracted as 10^{12} ~ 10^{13} cm⁻²eV⁻¹ with a band tail shape close to the conduction band, which is comparable to that in Si/SiO₂. However, ultra-thin 2D materials are more sensitive to interface disorder due to the reduced DOS , which drastically degrades the subthreshold properties. The multilayer MoS₂ is more suitable for device application due to its larger DOS . Having elucidated all the constituents in C_{total} quantitatively by C - V measurements, I - V characteristics are then well reproduced and understood by utilizing the drift current model. One of the physical origins for MIT is suggested to be the extrinsic outcome of the V_{TH} shift due to C_{it} and C_Q . Capacitance measurement is quite informative for detecting interface states and density of states in ultra-thin 2D materials, which allows us to understand device physics and improve device performance.

Acknowledgements

N. Fang was supported by a Grant-in-Aid for JSPS Research Fellows from the JSPS KAKENHI. This research was supported by the JSPS Core-to-Core Program, A. Advanced Research Networks, JSPS KAKENHI Grant Numbers JP25107004, JP16H04343, JP16K14446, and JP26886003, and JST PRESTO Grant Number JPMJPR1425, Japan.

References

- [1] Novoselov K, Jiang D, Schedin F, Booth T, Khotkevich V, Morozov S and Geim A 2005 Two-dimensional atomic crystals. *Proceedings of the National Academy of Sciences* **102** 10451-10453
- [2] Radisavljevic B, Radenovic A, Brivio J, Giacometti V and Kis A 2011 Single-layer MoS₂ transistors *Nature Nanotech* **6** 147-150
- [3] Baugher B, Churchill H, Yang Y and Jarillo-Herrero P 2013 Intrinsic electronic transport properties of high-quality monolayer and bilayer MoS₂ *Nano Letters* **13** 4212-4216
- [4] Kim S, Konar A, Hwang W, Lee J, Lee J, Yang J, Jung C, Kim H, Yoo J, Choi J, Jin Y, Lee S, Jena D, Choi W and Kim K 2012 High-mobility and low-power thin-film transistors based on multilayer MoS₂ crystals *Nature Communications* **3** 1011
- [5] Desai S, Madhvapathy S, Sachid A, Llinas J, Wang Q, Ahn G, Pitner G, Kim M, Bokor J, Hu C, Wong H and Javey A 2016 MoS₂ transistors with 1-nanometer gate lengths *Science* **354** 99-102
- [6] Kwon H, Kang H, Jang J, Kim S and Grigoropoulos C 2014 Analysis of flicker noise in two-dimensional multilayer MoS₂ transistors *Applied Physics Letters* **104** 083110
- [7] Ghatak S, Mukherjee S, Jain M, Sarma D and Ghosh A 2014 Microscopic origin of low frequency noise in MoS₂ field-effect transistors *APL Materials* **2** 092515
- [8] Radisavljevic B and Kis A 2013 Mobility engineering and a metal-insulator transition in monolayer MoS₂ *Nature Materials* **12** 815-820
- [9] Yu Z, Pan Y, Shen Y, Wang Z, Ong Z, Xu T, Xin R, Pan L, Wang B, Sun L, Wang J, Zhang G, Zhang Y, Shi Y and Wang X 2014 Towards intrinsic charge transport in monolayer molybdenum disulfide by defect and interface engineering *Nature Communications* **5** 5290
- [10] Chen X, Wu Z, Xu S, Wang L, Huang R, Han Y, Ye W, Xiong W, Han T, Long G, Wang Y, He Y, Cai Y, Sheng P and Wang N 2015 Probing the electron states and metal-insulator transition mechanisms in molybdenum disulphide vertical heterostructures *Nature Communications* **6** 6088
- [11] Qiu H, Xu T, Wang Z, Ren W, Nan H, Ni Z, Chen Q, Yuan S, Miao F, Song F, Long G, Shi Y, Sun L, Wang J and Wang X 2013 Hopping transport through defect-induced localized states in molybdenum disulphide *Nature Communications* **4** 2642
- [12] Hong J, Hu Z, Probert M, Li K, Lv D, Yang X, Gu L, Mao N, Feng Q, Xie L, Zhang J, Wu D, Zhang Z, Jin C, Ji W, Zhang X, Yuan J and Zhang Z 2015 Exploring atomic defects in molybdenum disulphide monolayers *Nature Communications* **6** 6293
- [13] Liu D, Guo Y, Fang L and Robertson J 2013 Sulfur vacancies in monolayer MoS₂ and its electrical contacts *Applied Physics Letters* **103** 183113
- [14] Nan F, Nagashio K and Toriumi A 2015 Subthreshold transport in mono- and multilayered MoS₂ FETs *Applied Physics Express* **8** 065203
- [15] Fang N, Nagashio K and Toriumi A 2016 Experimental detection of active defects in few layers MoS₂ through random telegraphic signals analysis observed in its FET characteristics *2D Materials* **4** 015035
- [16] Zhu W, Low T, Lee Y, Wang H, Farmer D, Kong J, Xia F and Avouris P 2014 Electronic transport and device prospects of

- monolayer molybdenum disulphide grown by chemical vapour deposition *Nature Communications* **5** 3087
- [17] Takenaka M, Ozawa Y, Han J and Takagi S 2016 Quantitative evaluation of energy distribution of interface trap density at MoS₂ MOS interfaces by The Terman Method. *International Electron Devices Meeting (IEDM) Tech. Dig.* 5-8
- [18] Luryi S 1988 Quantum capacitance devices *Applied Physics Letters* **52** 501-503
- [19] Ma N and Jena D 2015 Carrier statistics and quantum capacitance effects on mobility extraction in two-dimensional crystal semiconductor field-effect transistors *2D Materials* **2** 015003
- [20] Nicollian E and Brews J 2003 *MOS (metal oxide semiconductor) physics and technology* (Hoboken: Wiley-Interscience)
- [21] Martens K, Chui C, Brammertz G, De Jaeger B, Kuzum D, Meuris M, Heyns M, Krishnamohan T, Saraswat K, Maes H and Groeseneken G 2008 On the correct extraction of interface trap density of MOS devices with high-mobility semiconductor substrates *IEEE Transactions on Electron Devices* **55** 547-556
- [22] Park S, Kim S, Choi Y, Kim M, Shin H, Kim J and Choi W 2016 Interface properties of atomic-layer-deposited Al₂O₃ thin films on ultraviolet/ozone-treated multilayer MoS₂ Crystals *ACS Applied Materials & Interfaces* **8** 11189-11193
- [23] Xia P, Feng X, Ng R, Wang S, Chi D, Li C, He Z, Liu X and Ang K 2017 Impact and origin of interface states in MOS capacitor with monolayer MoS₂ and HfO₂ high-k dielectric *Scientific Reports* **7** 40669
- [24] Kuiri M, Kumar C, Chakraborty B, Gupta S, Naik M, Jain M, Sood A and Das A 2015 Probing 2D black phosphorus by quantum capacitance measurements *Nanotechnology* **26** 485704
- [25] Ninomiya N, Mori T, Uchida N, Watanabe E, Tsuya D, Moriyama S, Tanaka M and Ando A 2015 Fabrication of high-k/metal-gate MoS₂ field-effect transistor by device isolation process utilizing Ar-plasma etching *Japanese Journal of Applied Physics* **54** 046502
- [26] Mori T, Ninomiya N, Kubo T, Uchida N, Watanabe E, Tsuya D, Moriyama S, Tanaka M and Ando A 2016 Characterization of effective mobility and its degradation mechanism in MoS₂ MOSFETs *IEEE Transactions on Nanotechnology* **15** 651-656
- [27] Takahashi N and Nagashio K 2016 Buffer layer engineering on graphene via various oxidation methods for atomic layer deposition *Applied Physics Express* **9** 125101
- [28] Kurabayashi S and Nagashio K 2017 Transport properties of the top and bottom surfaces in monolayer MoS₂ grown by chemical vapor deposition *Nanoscale* **9** 13264
- [29] Heiman F and Warfield G 1965 The effects of oxide traps on the MOS Capacitance. *IEEE Trans. Electron Devices* **12** 167-178
- [30] Brammertz G, Martens K, Sioncke S, Delabie A, Caymax M, Meuris M and Heyns M 2007 Characteristic trapping lifetime and capacitance-voltage measurements of GaAs metal-oxide-semiconductor structures *Applied Physics Letters* **91** 133510
- [31] Takagi S and Toriumi A 1995 Quantitative understanding of inversion-layer capacitance in Si MOSFET's *IEEE Transactions on Electron Devices* **42** 2125-2130
- [32] John D, Castro L and Pulfrey D 2004 Quantum capacitance in nanoscale device modeling *Journal of Applied Physics* **96** 5180-5184
- [33] Kanayama K, Nagashio K, Nishimura T and Toriumi A 2014 Large Fermi energy modulation in graphene transistors with high-pressure O₂-annealed Y₂O₃ topgate insulators *Applied Physics Letters* **104** 083519
- [34] Kanayama K and Nagashio K 2015 Gap state analysis in electric-field-induced band gap for bilayer graphene *Scientific Reports* **5** 15789
- [35] Schroder D K 2006 *Semiconductor material and device characterization* (John Wiley & Sons)
- [36] Martens K, Wang W, De Keersmaecker K, Borghs G, Groeseneken G and Maes H 2007 Impact of weak Fermi-level pinning on the correct interpretation of III-V MOS C-V and G-V characteristics *Microelectronic Engineering* **84** 2146-2149
- [37] Martens K, Wang W, Dimoulas A, Borghs G, Meuris M, Groeseneken G and Maes H 2007 Determining weak Fermi-level pinning in MOS devices by conductance and capacitance analysis and application to GaAs MOS devices *Solid-State Electronics* **51** 1101-1108
- [38] Berglund C 1966 Surface states at steam-grown silicon-silicon dioxide interfaces *IEEE Transactions on Electron Devices* ED-**13** 701-705
- [39] White M and Cricchi J 1972 Characterization of thin-oxide MNOS memory transistors *IEEE Transactions on Electron Devices* **19** 1280-1288
- [40] Sakurai T and Sugano T 1981 Theory of continuously distributed trap states at Si-SiO₂ interfaces *Journal of Applied Physics* **52** 2889-2896
- [41] Ryan J, Southwick R, Campbell J, Cheung K, Young C and Suehle J 2011 On the "U-shaped" continuum of band edge states at the Si/SiO₂ interface *Applied Physics Letters* **99** 223516
- [42] Matsubara H, Sasada T, Takenaka M and Takagi S 2008 Evidence of low interface trap density in GeO₂/Ge metal-oxide-semiconductor structures fabricated by thermal oxidation *Applied Physics Letters* **93** 032104
- [43] Lee C H, Nishimura T, Nagashio K, Kita K and Toriumi A 2011 High-electron-mobility Ge/GeO₂ n-MOSFETs with two-step oxidation. *IEEE Trans. Electron Devices* **58** 1295-1301
- [44] Hasegawa H 1986 Unified disorder induced gap state model for insulator-semiconductor and metal-semiconductor interfaces *Journal of Vacuum Science & Technology B: Microelectronics and Nanometer Structures* **4** 1130
- [45] Pantelides S 2013 *The Physics of SiO₂ and Its Interfaces* (Elsevier Science: Burlington)
- [46] Wilson J A, and Yoffe A D 1969 The transition metal dichalcogenides discussion and interpretation of the observed optical, electrical and structural properties. *Adv. Phys.* **18**, 193-335.
- [47] Zou X, Wang j, Chiu C -H, Wu Y, Xiao X, Jiang C, Wu W -W, Mai L, Chen T, Li J, Ho J C and Lia L 2014 Interface engineering for high-performance top-gated MoS₂ field-effect transistors. *Advanced Materials* **26** 6255-6261
- [48] Lee G -H, Kim Y D, Arefe G, Xhang X, Lee C -H, Ye F, Watanabe K, Taniguchi T, Kim P and Hone J 2015 Highly stable, dual-gated MoS₂ transistors encapsulated by hexagonal boron nitride with gate-controllable contact, resistance, and threshold voltage. *ACS nano* **9** 7019-7026
- [49] Komsa H, Kurasch S, Lehtinen O, Kaiser U and Krasheninnikov A 2013 From point to extended defects in two-dimensional

- MoS₂: Evolution of atomic structure under electron irradiation *Physical Review B* **88** 035301
- [50] Cui X, Lee G, Kim Y, Arefe G, Huang P, Lee C, Chenet D, Zhang X, Wang L, Ye F, Pizzocchero F, Jessen B, Watanabe K, Taniguchi T, Muller D, Low T, Kim P and Hone J 2015 Multi-terminal transport measurements of MoS₂ using a van der Waals heterostructure device platform *Nature Nanotechnology* **10** 534-540

Supplementary data

Band tail interface states and quantum capacitance in a monolayer molybdenum disulfide field-effect-transistor

Nan Fang¹ and Kosuke Nagashio^{1,2}

¹Department of Materials Engineering, The University of Tokyo, Tokyo 113-8656, Japan

²PRESTO, Japan Science and Technology Agency (JST), Japan

E-mail: nan@adam.t.u-tokyo.ac.jp, nagashio@material.t.u-tokyo.ac.jp

Supplementary data

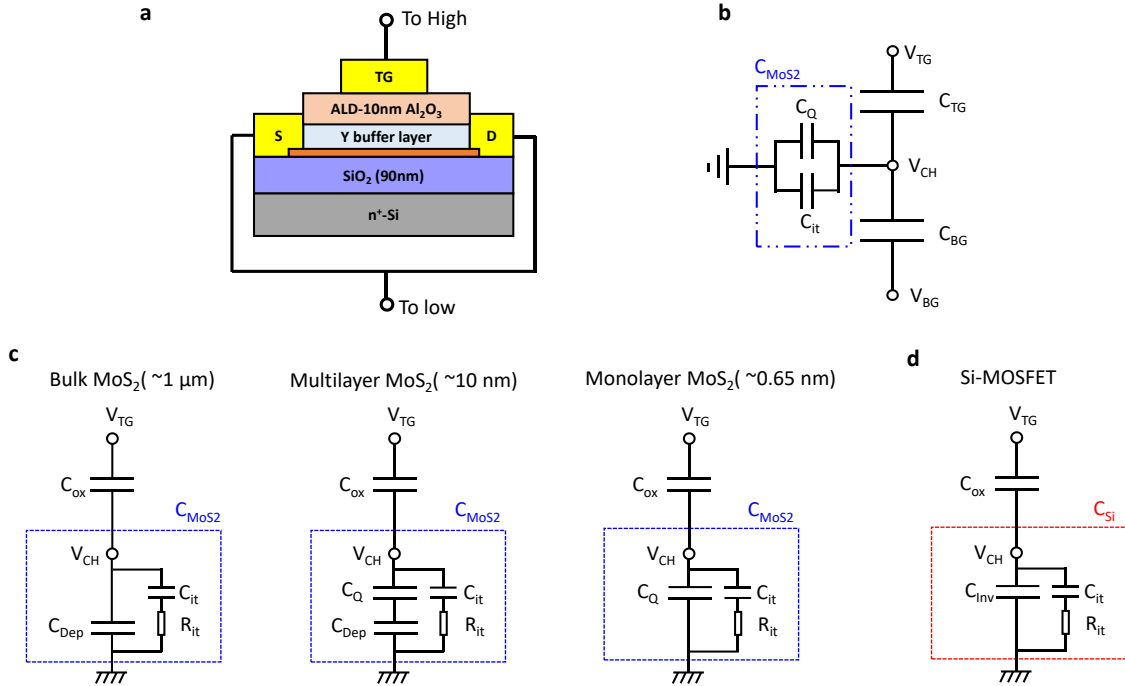


Figure S1. (a) The configuration of capacitance measurement for MoS_2 FET. (b) Simplified equivalent circuit of monolayer MoS_2 in dual-gate I - V measurement. (c) Three different equivalent circuits for the MoS_2 FET with different channel thickness for C - V measurement. C_{Dep} is expressed as ϵ_s/W_D , where ϵ_s is dielectric constant of semiconductor and W_D is depletion width. It should be noted that MoS_2 FET operates at the accumulation region and turns off at the depletion region. Therefore, for all three cases, the inversion layer capacitance (C_{Inv}) is not shown. (d) Si MOSFET operates at the inversion region. Therefore, for the C - V measurement of Si-MOSFET structure, the semiconductor capacitance is composed of C_{Inv} , instead of C_{Q} .

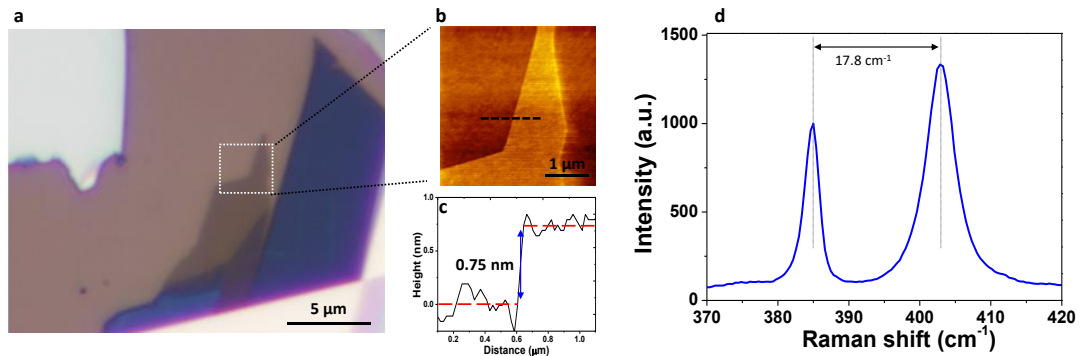


Figure S2. Thickness identification of MoS_2 . (a) Optical image of MoS_2 with different layer numbers. Monolayer can be simply identified in this image by the contrast, which is then confirmed by AFM and Raman spectroscopy. (b) AFM image of the white-dashed rectangle area in (a). (c) Height profile along the dashed line in (b). The height of monolayer MoS_2 is 0.75 nm. (d) Raman spectroscopy of typical measured monolayer MoS_2 . The wavenumber between the two peaks (E_{2g} , A_{1g}) is 17.8 cm^{-1} , which proves to be monolayer MoS_2 .

Supplementary data

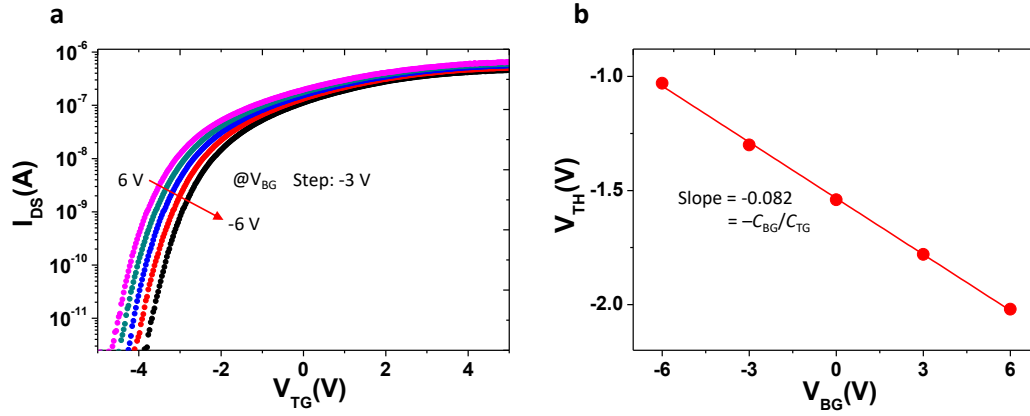


Figure S3. (a) $I_{DS}-V_{TG}$ characteristics for sample 3 with $V_{DS} = 0.1$ V at different V_{BG} . V_{BG} ranges from 6~-6 V with a step of 3 V. (b) The trace of V_{TH} observed for the V_{TG} sweep as a function of V_{BG} . The V_{TH} position is controlled by the relative ratio of capacitive coupling between the top and back gates with a MoS₂ channel (Detailed derivation are shown below). Therefore, the slope shown in (b) corresponds to $-C_{BG}/C_{TG}$, where C_{BG} and C_{TG} are the back and top gate capacitances, respectively. Because C_{BG} is $0.038 \mu\text{F}/\text{cm}^2$ for the 90-nm SiO₂ with $k_{\text{SiO}_2} = 3.9$, C_{TG} can be estimated to be $0.46 \mu\text{F}/\text{cm}^2$.

Based on equivalent circuit in figure S1b, the total charge in the channel is induced by both top gate and bottom gate.

$$V_{CH}C_{\text{MoS}_2} = (V_{TG} - V_{CH})C_{TG} + (V_{BG} - V_{CH})C_{BG}, \quad (1)$$

where C_{MoS_2} is capacitance of MoS₂, which consists of C_Q and C_{it} in parallel. Carrier density is constant in principle when source/drain current is kept unchanged. As a result, V_{CH} and C_{MoS_2} are also constant¹. Therefore, after transformation,

$$\text{Const.} = V_{CH}(C_{\text{MoS}_2} + C_{TG} + C_{BG}) = V_{TG}C_{TG} + V_{BG}C_{BG}. \quad (2)$$

By modulating top gate and bottom gate simultaneously at constant source/drain current, $V_{BG} \rightarrow V_{BG} + \Delta V_{BG}$, $V_{TG} \rightarrow V_{TG} + \Delta V_{TG}$.

Equation 2 turns to be

$$\text{Const.} = (V_{TG} + \Delta V_{TG})C_{TG} + (V_{BG} + \Delta V_{BG})C_{BG}. \quad (3)$$

By comparing equation 2 and 3,

$$\Delta V_{TG}C_{TG} + \Delta V_{BG}C_{BG} = 0, \quad (4)$$

or

$$-C_{BG}/C_{TG} = \Delta V_{TG}/\Delta V_{BG}. \quad (5)$$

Experimentally, source/drain current is kept as constant below or close to the current level at V_{TH} due to high sensitivity of carrier density as a function of gate bias at subthreshold region.

Supplementary data

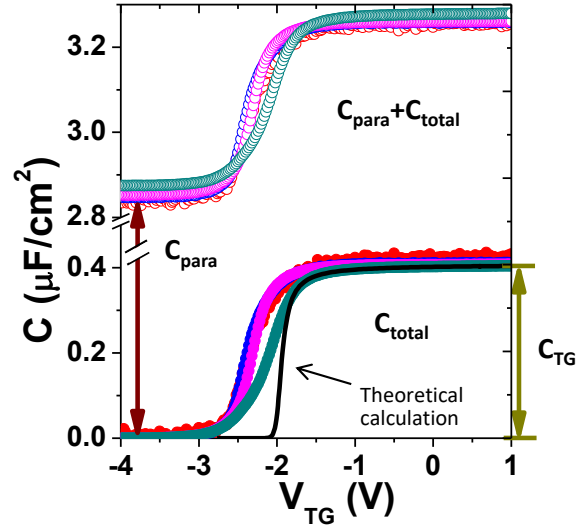


Figure S4. The open circles indicate the measured raw C - V data at different frequencies for sample 1, which includes C_{para} . It should be noted that the back gate voltage was not applied, just floating. Ideally, the measured capacitance (C_{total}) is zero at the deep depletion region, that is, the off state for I - V , and saturates asymptotically to C_{TG} at the strong accumulation region because C_{Q} ($\sim 84 \mu\text{F cm}^{-2}$) for monolayer MoS₂ at this region is much larger than C_{TG} . Therefore, all of the C - V curves at different frequencies were shifted to start from zero at the off state. The solid circles indicate C_{total} after removing C_{para} . After this correction, C_{total} saturate asymptotically to C_{TG} at the strong accumulation region. Therefore, C_{TG} is extracted at accumulation region, which is consistent with C_{TG} estimated from I - V in figure S2 within the 10% error. Reversely, the black line is theoretical calculation based on $1/C_{\text{total}} = 1/C_{\text{Q}} + 1/C_{\text{TG}}$, where C_{Q} was calculated using eq. (3) in the main text and the constant C_{TG} value obtained above was used in this calculation. At the saturation region, theoretical calculation successfully reproduced the C - V data, suggesting that the present correction is reasonable.

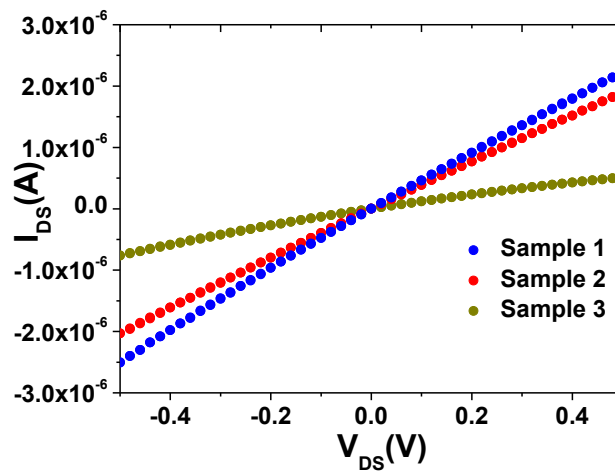


Figure S5. I_{DS} - V_{DS} curve without gate bias at 300 K. The linear properties indicate good ohmic contact for all three samples.

Supplementary data

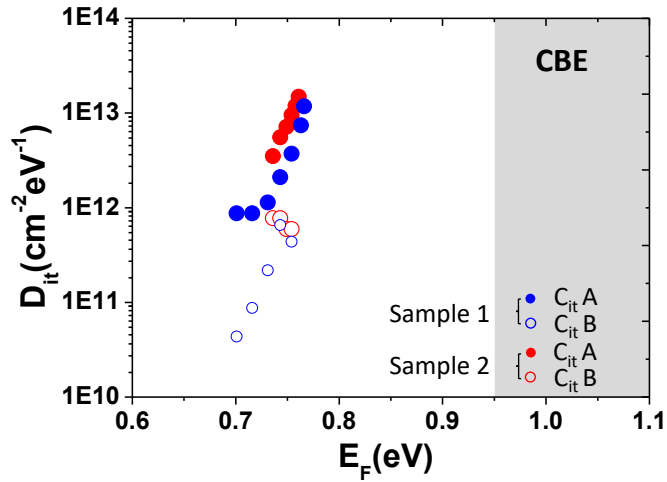


Figure S6. D_{it} is shown as a function of E_F by referring to E_F - C_Q correlation, which is discussed in the Quantum capacitance analysis section. D_{itA} is the main interface states which shows tail distribution close to conduction band edge and dominate interface properties. D_{itB} is much smaller than D_{itA} and not always observed. Thus, D_{itB} is not discussed for samples 1, 2 in the main text.

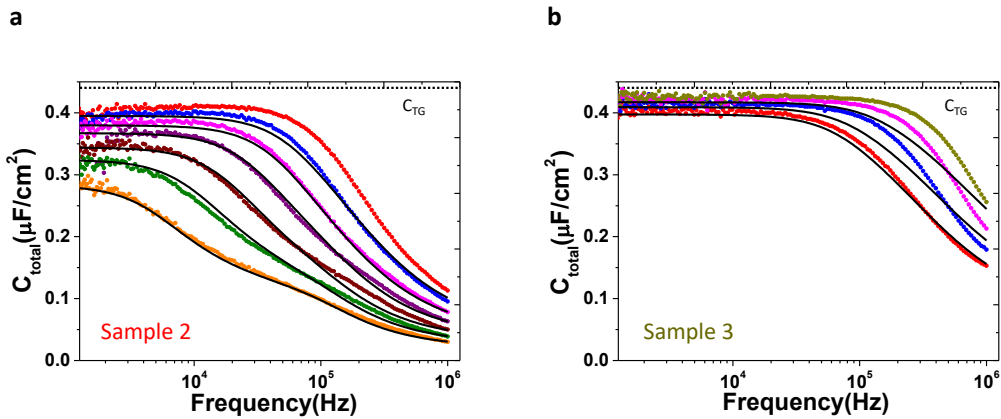


Figure S7. (a) Capacitance as a function of frequency for sample 2 at fixed V_{TG} (-3.8 ~ -3.2 V with the step of 0.1 V). (b) Capacitance as a function of frequency for sample 3 at fixed V_{TG} (-2.4 ~ -1.5 V with the step of 0.3 V). Solid circles are experimental results and black solid lines are fitting by using eq. (1) in the main text.

Supplementary data

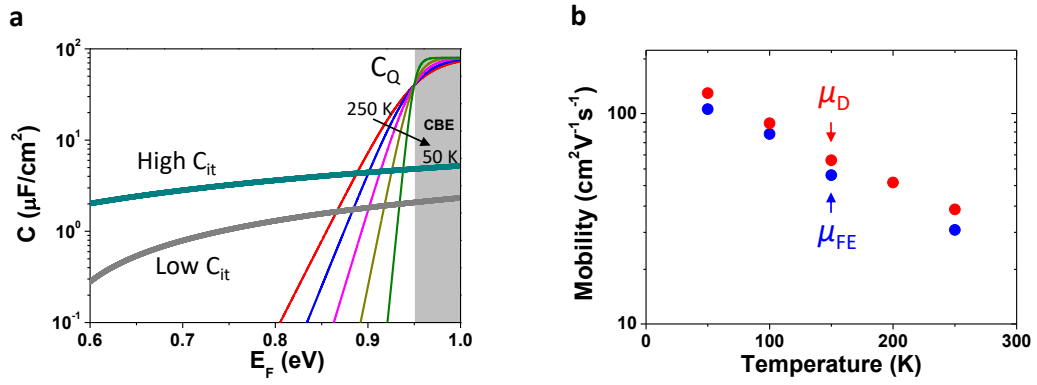


Figure S8. (a) C_{it} of with different levels and calculated C_Q as a function of E_F at different temperatures (50 ~ 250 K) used for I - V modelling based on back-gate monolayer MoS_2 FET on 90-nm SiO_2/n^+ -Si substrate. Ideally, C_{it} does not show any temperature dependence, while C_Q shows clear temperature dependence from Fermi distribution. It should be noted that the temperature dependence of C_Q shown in figure 6a,b in the main text is shown as a function of V_{TG} . (b) Comparison of μ_{FE} estimated from the experimental I - V data and μ_D used as fitting parameter in the modelling.

Supplementary data

Note S1. D_{it} extraction from S.S. in I - V .

The definition of S.S at subthreshold region is²

$$S.S. = (\ln 10) \frac{dV_G}{d(\ln I_D)} = (\ln 10) \frac{k_B T}{e} \frac{dV_G}{d(V_{CH})}. \quad (6)$$

Based on equivalent circuit and considering the fact that C_Q at subthreshold region is much smaller than C_{ox} and C_{it} ,

$$\frac{d(V_G)}{d(V_{CH})} = \frac{C_{TG} + C_Q + C_{it}}{C_{TG}} \approx \frac{C_{TG} + C_{it}}{C_{TG}}. \quad (7)$$

Since S.S. is related with V_{TG} experimentally,

$$S.S.(V_{TG}) = (\ln 10) \frac{k_B T}{e} \frac{C_{TG} + C_{it}(V_{TG})}{C_{TG}}, \quad (8)$$

D_{it} is then extracted as a function of V_{TG} .

Table S1. Physical properties extracted from measured devices.

	Monolayer Sample 1	Monolayer Sample 2	Monolayer Sample 3	Monolayer T-dependence	Multilayer ~9 nm
Gate area (μm^2)	143	105	133	37	418
C_{ox} by IV ($\mu\text{F}/\text{cm}^2$)	0.38		0.46	0.34	
C_{ox} by CV ($\mu\text{F}/\text{cm}^2$)	0.41	0.44	0.44	0.36	0.31
Mobility at 300 K ($\text{cm}^2\text{V}^{-1}\text{s}^{-1}$)	9.5	6.0	2.0	10.0	33.0
S.S. at 300 K (mV/dec)	110	300	300	240	160

C_{TG} values for three samples are different because they are from different batches.

REFERENCES

1. Ma, N.; Jena, D. Carrier Statistics and Quantum Capacitance Effects on Mobility Extraction in Two-Dimensional Crystal Semiconductor Field-Effect Transistors. *2D Materials* **2015**, *2*, 015003.
2. Nicollian, E.; Brews, J. *MOS (Metal Oxide Semiconductor) Physics And Technology*; Wiley-Interscience: Hoboken, 2003.
3. Heiman, F.; Warfield, G. The Effects of Oxide Traps on The MOS Capacitance. *IEEE Trans. Electron Devices* **1965**, *12*, 167-178.